AIMS Mathematics, 10(5): 11111–11130.
DOI: 10.3934/math.2025504
Received: 14 January 2025
Revised: 03 May 2025
Accepted: 08 May 2025
Published: 15 May 2025

https://www.aimspress.com/journal/Math

Research article

Bifurcation analysis and stochastic optical solutions to the stochastic nonlinear Kodama equation in nonlinear optics

Sofian T. Obeidat[1], Doaa Rizk[2,*], Wael W. Mohammed[1] and Adel Elmandouh[3,4]

[1] Department of Mathematics, College of Science, University of Ha'il, Ha'il 2440, Saudi Arabia

[2] Department of Mathematics, College of Science, Qassim University, Saudi Arabia

[3] Department of Mathematics and Statistics, College of Science, King Faisal University, P.O. Box 400, Al-Ahsa 31982, Saudi Arabia

[4] Department of Mathematics, Faculty of Science, Mansoura University, Mansoura 35516, Egypt

* **Correspondence:** Email: d.hussien@qu.edu.sa.

Abstract: We consider the stochastic nonlinear Kodama equation (SNLKE) driven by multiplicative white noise. A specific wave transformation is applied to convert this system into a one-dimensional conservative Hamiltonian system. We analyze the bifurcation of this system and present its phase portrait. Additionally, a brief description of the phase portrait is provided, along with an illustration of the phase orbit degeneracy depending on the bifurcation parameter. Bifurcation allows us to deduce that changing the parameter values can have a substantial influence on nonlinear optics and mathematical physics as well as the dynamics of the optical soliton solutions of the Kodama equation. Using the conserved quantity, we derive new traveling wave solutions for the SNLKE. In the absence of noise, we recover certain wave solutions for the deterministic case. Furthermore, we examine the influence of multiplicative white noise on the exact solutions of the SNLKE, with some of the obtained solutions visualized graphically.

Keywords: exact solutions; simulation; mathematical model; qualitative theory; white noise; stabilizes by noise
Mathematics Subject Classification: 35A20, 35Q51, 60H10, 60H15

1. Introduction

Stochastic nonlinear evolution equations (SNLEEs) play a crucial role in a wide range of scientific disciplines, including physics, biology, chemistry, economics, finance, climate science, and many others [1, 2]. Therefore, finding solutions to these equations is important because it allows researchers

to make predictions about the behavior of a system under different conditions, and to optimize strategies for controlling and manipulating the system.

Recently, there are several analytical methods that can be employed to find solutions to nonlinear evolution equations (NLEEs), ranging from simple separation of variables to more advanced techniques such as the $exp(-\phi(\varsigma))$-expansion method [3], the Riccati equation method [4], the qualitative theory of dynamical systems [5–7], the sine-cosine method [8], the (G'/G)-expansion [9, 10], the sine-Gordon expansion technique [11], the Jacobi elliptic function expansion [12], the F-expansion method [13], the Kudryashov's method [14], the Hirota Bilinear method [15], the direct algebraic equation method [16], the modified exp-function method [17], the Elzaki transform [18], etc. By understanding these analytical methods and their applications, mathematicians and scientists can tackle complex NLEEs and gain valuable insights into the behavior of the solutions.

Optical solutions are exact or approximate analytical solutions of nonlinear partial differential equations (PDEs) that model light wave propagation in optical systems. These solutions play a vital role in areas such as nonlinear optics, fiber optics, and laser physics, where wave dynamics are influenced by nonlinear effects like self-phase modulation, dispersion, and diffraction. Optical solutions are classified into different types. Optical soliton solutions are localized waves that maintain their shape during propagation. Periodic and super-periodic optical solutions refer to repeating waveforms that appear in optical lattices and photonic crystals. Breather optical solutions are localized waves that periodically grow and decay in amplitude. Rogue optical wave solutions are extreme localized waves that emerge in optical fibers due to modulation instability.

In this paper we consider the stochastic nonlinear Kodama equation (SNLKE) as follows:

$$i\mathcal{G}_t + \mathcal{G}_{xx} + i\mathcal{G}_{xxx} + \ell_1|\mathcal{G}|^2\mathcal{G} + \ell_2|\mathcal{G}|^2\mathcal{G}_x + i\ell_3\mathcal{G}^2\mathcal{G}_x^* = i\sigma\mathcal{G} \circ \mathcal{B}_t, \tag{1.1}$$

where $\mathcal{G} = \mathcal{G}(x,t)$ represents the complex function, $i^2 = -1$, $\overset{*}{\mathcal{G}}$ is the complex conjugate of $\mathcal{G}$, ℓ_1, ℓ_2 and ℓ_3 are arbitrary constants, σ is the noise amplitude. $\mathcal{B} = \mathcal{B}(t)$ is the Brownian motion, $\mathcal{B}_t = \frac{\partial \mathcal{B}}{\partial t}$ and $\mathcal{G} \circ \mathcal{B}_t$ is a multiplicative noise in the Stratonovich sense. In this paper, we only consider the condition in which noise is a spatial constant. It is very crucial at this point to establish the definition of a Brownian motion. The stochastic process $\mathcal{B}(t)$ is called Brownian motion if it satisfies the following conditions: (I) $\mathcal{B}(0) = 0$, (II) $\mathcal{B}(t)$ has continuous trajectories, (III) $\{\mathcal{B}(t)\}_{t=0}^{\infty}$ has stationary, independent increments, (IV) the $\mathcal{B}(t)$ has a normal distribution. When we put $\sigma = 0$, we have the deterministic nonlinear Kodama equation [19]:

$$i\mathcal{G}_t + \mathcal{G}_{xx} + i\mathcal{G}_{xxx} + \ell_1|\mathcal{G}|^2\mathcal{G} + \ell_2|\mathcal{G}|^2\mathcal{G}_x + i\ell_3\mathcal{G}^2\mathcal{G}_x^* = 0. \tag{1.2}$$

The nonlinear Kodama equation (NLKE) (1.2), also known as the nonlinear Schrödinger equation, is an important mathematical equation used in the field of nonlinear optics. Nonlinear optics is the study of how materials interact with light in a nonlinear way, leading to phenomena such as harmonic generation, self-focusing, and soliton formation. The Kodama equation plays a crucial role in understanding and predicting these nonlinear optical phenomena. Moreover, the Kodama equation is used in the study of optical fiber communications. Optical fibers are widely used for long-distance data transmission due to their low attenuation and high data-carrying capacity. Nonlinear effects in optical fibers, such as self-phase modulation and four-wave mixing, can degrade the quality of the transmitted data. The Kodama equation helps researchers model and mitigate these nonlinear effects,

allowing for more efficient and reliable optical communications systems. Due to the significance of the NLKE (1.2), many authors have acquired its solutions by applying many different methods including the generalized Jacobi elliptic method [20], the ansatz method [21], the modified Jacobi method [22], the planar dynamical system and Lie symmetries group [23], the generalized Riccati equation method [24]. While the stochastic exact solutions for SNLKE (1.1) have been obtained by using the (G'/G)-expansion method and mapping method [25].

This article's goal is to utilize the bifurcation method to find the exact solutions of the SNLKE (1.1) driven by multiplicative white noise. The phase portrait of Eq (1.1) is examined and analyzed using the qualitative theory of dynamical systems. In order to investigate the impact of multiplicative white noise on these solutions, the solutions are also graphically displayed for a range of noise strength parameter values.

The rest of this paper is structured as follows: Section 2 introduces a wave transformation that reduces the SNLKE (1.1) to a Hamiltonian system with a single degree of freedom. Section 3 presents a bifurcation study using Hamiltonian concepts. In Section 4, we provide new stochastic traveling wave solutions for the SNLKE (1.1). Section 5 investigates the quasi-periodic behavior after introducing certain periodic external effects. Finally, Section 6 presents the conclusion based on the results obtained.

2. Mathematical analysis

In this section, we obtain the traveling wave equation using a suitable transformation. After that, we obtain a Hamiltonian system with a single degree of freedom. To obtain the wave equation, we assume that the solution to Eq (1.1) takes the following form:

$$\mathcal{G}(x,t) = \mathcal{W}(\xi)e^{i\Theta+\sigma\mathcal{B}(t)-\sigma^2 t},\ \Theta = \theta_1 x + \theta_2 t,\ \ \xi = \xi_1 x + \xi_2 t, \tag{2.1}$$

where $\mathcal{W}$ is a real deterministic function, ξ_i and θ_i are free parameters for $i = 1, 2$. We see that

$$\begin{aligned} \mathcal{G}_t &= [\zeta_2\mathcal{W}' + i\theta_2\mathcal{W} + \sigma\mathcal{W}\mathcal{W}_t + \frac{1}{2}\sigma^2\mathcal{W} - \sigma^2\mathcal{W}]e^{i\Theta+\sigma\mathcal{B}(t)-\sigma^2 t} \\ &= [\zeta_2\mathcal{W}' + i\theta_2\mathcal{W} + \sigma\mathcal{W}\circ\mathcal{W}_t]e^{i\Theta+\sigma\mathcal{B}(t)-\sigma^2 t}, \end{aligned} \tag{2.2}$$

where $+\frac{1}{2}\sigma^2\mathcal{W}$ is the Itô correction term, and

$$\begin{aligned} \mathcal{G}_x &= (\zeta_1\mathcal{W}' + i\theta_1\mathcal{W})e^{i\Theta+\sigma\mathcal{B}(t)-\sigma^2 t}, \\ \mathcal{G}_{xx} &= (\zeta_1^2\mathcal{W}'' + 2i\theta_1\zeta_1\mathcal{W}' - \theta_1^2\mathcal{W})e^{i\Theta+\sigma\mathcal{B}(t)-\sigma^2 t}, \\ \mathcal{G}_{xxx} &= (\zeta_1^3\mathcal{W}''' + 3i\theta_1\zeta_1^2\mathcal{W}'' - 3\theta_1^2\zeta_1\mathcal{W}' - i\theta_1^3\mathcal{W})e^{i\Theta+\sigma\mathcal{B}(t)-\sigma^2 t}. \end{aligned} \tag{2.3}$$

Substituting Eqs (2.2) and (2.3) into Eq (1.1), we have for the real part

$$(\zeta_1^2 - 3\ell_1\theta_1\zeta_1^2)\mathcal{W}'' + (\ell_1\theta_1^3 - \theta_2 - \theta_1^2)\mathcal{W} + (\ell_1 - \ell_2\theta_1 + \ell_3\theta_1)\mathcal{W}^3 e^{2\sigma\mathcal{B}(t)-2\sigma^2 t} = 0, \tag{2.4}$$

and for the imaginary part,

$$\ell_1\zeta_1^3\mathcal{W}''' + (\zeta_2 + 2\theta_1\zeta_1 - 3\ell_1\theta_1^2\zeta_1)\mathcal{W}' + \zeta_1(\ell_2 + \ell_3)\mathcal{W}^2\mathcal{W}' e^{2\sigma\mathcal{B}(t)-2\sigma^2 t} = 0. \tag{2.5}$$

Taking the expectation $\mathbb{E}(\cdot)$ on both sides into Eqs (2.4) and (2.5), we have

$$(\zeta_1^2 - 3\ell_1\theta_1\zeta_1^2)\mathcal{W}'' + (\ell_1\theta_1^3 - \theta_2 - \theta_1^2)\mathcal{W} + (\ell_1 - \ell_2\theta_1 + \ell_3\theta_1)\mathcal{W}^3 e^{-2\sigma^2 t}\mathbb{E}(e^{2\sigma\mathcal{B}(t)}) = 0, \tag{2.6}$$

and

$$\ell_1\zeta_1^3\mathcal{W}'''' + (\zeta_2 + 2\theta_1\zeta_1 - 3\ell_1\theta_1^2\zeta_1)\mathcal{W}' + \zeta_1(\ell_2 + \ell_3)\mathcal{W}^2\mathcal{W}' e^{-2\sigma^2 t}\mathbb{E}(e^{2\sigma\mathcal{B}(t)}) = 0, \tag{2.7}$$

where $\mathcal{W}$ is a real deterministic. Since $\mathcal{B}(t)$ is a normal distribution, then $\mathbb{E}(e^{\sigma\mathcal{B}(t)}) = e^{\frac{1}{2}\sigma^2 t}$ for $\sigma > 0$ (for details, see [26]). Therefore, Eqs (2.6) and (2.7) become

$$(\zeta_1^2 - 3\ell_1\theta_1\zeta_1^2)\mathcal{W}'' + (\ell_1\theta_1^3 - \theta_2 - \theta_1^2)\mathcal{W} + (\ell_1 - \ell_2\theta_1 + \ell_3\theta_1)\mathcal{W}^3 = 0, \tag{2.8}$$

and

$$\ell_1\zeta_1^3\mathcal{W}'''' + (\zeta_2 + 2\theta_1\zeta_1 - 3\ell_1\theta_1^2\zeta_1)\mathcal{W}' + \zeta_1(\ell_2 + \ell_3)\mathcal{W}^2\mathcal{W}' = 0. \tag{2.9}$$

Integrating (2.9) once and putting the integration constant equal to zero, we obtain

$$\ell_1\zeta_1^3\mathcal{W}'' + (\zeta_2 + 2\theta_1\zeta_1 - 3\ell_1\theta_1^2\zeta_1)\mathcal{W} + \zeta_1(\ell_2 + \ell_3)\mathcal{W}^3 = 0. \tag{2.10}$$

Hence, Eqs (2.8) and (2.10) are equal with the following constraint conditions:

$$\theta_1 = \frac{\ell_2 + \ell_3 - \ell_1^2}{2\ell_1\ell_2 + 4\ell_1\ell_3}, \text{ and } \theta_2 = \frac{8\theta_1^2\ell_1\zeta_1(1 - \theta_1\ell_1) - 2\theta_1\zeta_1 + \zeta_2(3\theta_1\ell_1 - 1)}{\ell_1\zeta_1}.$$

Rewriting Eq (2.10) with the previous conditions, we have

$$\mathcal{W}''(\xi) + r\mathcal{W}(\xi) + s\mathcal{W}^3(\xi) = 0, \tag{2.11}$$

where r and s are given by

$$r = \frac{\zeta_2 + 2\theta_1\zeta_1 - 3\ell_1\theta_1^2\zeta_1}{\ell_1\zeta_1^3}, \text{ and } \quad s = \frac{\ell_2 + \ell_3}{\ell_1\zeta_1^2}. \tag{2.12}$$

Equation (2.11) can be written as a dynamical system in the form

$$\begin{aligned} \mathcal{W}' &= \mathcal{Y}, \\ \mathcal{Y}' &= -\mathcal{W}(r + s\mathcal{W}^2). \end{aligned} \tag{2.13}$$

Because the system (2.13) is formed from the next Hamiltonian function and $\text{div}(\mathcal{W}', \mathcal{Y}') = 0$, the system (2.13) is a conservative Hamiltonian system.

$$\mathcal{H} = \frac{1}{2}\mathcal{Y}^2 + \frac{r}{2}\mathcal{W}^2 + \frac{s}{4}\mathcal{W}^4, \tag{2.14}$$

using canonical Hamilton equations [27]. Physically, the Hamiltonian (2.14) is the one-dimensional motion of a unit-mass particle under the influence of a potential function characterized by two parameters

$$V(\mathcal{W}) = \frac{r}{2}\mathcal{W}^2 + \frac{s}{4}\mathcal{W}^4. \tag{2.15}$$

Therefore, solving Eq (2.14) is equivalent to determining a solution for the Hamiltonian system (2.13). Scince, $\frac{\partial \mathcal{H}}{\partial \xi} = 0$, the Hamiltonian (2.14) is constant of motion, meaning it maintains a fixed value along the phase plane orbits. Thus, we have

$$\frac{1}{2}\mathcal{Y}^2 + \frac{r}{2}\mathcal{W}^2 + \frac{s}{4}\mathcal{W}^4 = p, \tag{2.16}$$

where p is a constant that plays a significant role, as will be shown later. Using the system (2.13) and the constant of motion (2.16) and separating the variable provide

$$\frac{\mathrm{d}\mathcal{W}}{\sqrt{f(\mathcal{W})}} = \pm \mathrm{d}\xi, \tag{2.17}$$

where $f(\mathcal{W})$ is a quartic polynomial given by

$$f(\mathcal{W}) = 2p - r\mathcal{W}^2 - \frac{s}{2}\mathcal{W}^4. \tag{2.18}$$

3. Bifurcation analysis

The possible values of the parameters p, r, and s must be identified in order to integrate both sides of Eq (2.17). To discover these parameter ranges and categorize the different kinds of solutions before solving the equation, a bifurcation analysis must be carried out.

We utilize Hamiltonian approaches to determine the system's equilibrium points (2.13) and examine their characteristics [27]. The equilibrium points, or $(\mathcal{W}_0, 0)$, are the critical positions for the potential function (2.15), where $\mathcal{W}_0$ is a solution for

$$\frac{\mathrm{d}V}{\mathrm{d}\mathcal{W}} = \mathcal{W}_0(r + s\mathcal{W}_0^2) = 0. \tag{3.1}$$

Hence, if $rs > 0$, the system (2.13) has a single equilibrium point, $O = (0, 0)$. However, if $rs < 0$, the system has three equilibrium points: $O = (0, 0)$ and $Q_{1,2} = (\pm\sqrt{\frac{-r}{s}}, 0)$. According to Lagrange's theorem, the equilibrium point of a conservative Hamiltonian system is either stable (a center) if it corresponds to a minimum of the potential function (2.15), or unstable (a saddle point) if it corresponds to a maximum of the potential function (2.15). Thus, we calculate

$$\frac{\mathrm{d}^2V}{\mathrm{d}\mathcal{W}^2}|_O = r, \qquad \frac{\mathrm{d}^2V}{\mathrm{d}\mathcal{W}^2}|_{Q_{1,2}} = -2r. \tag{3.2}$$

Thus, we have:

(a) If $rs > 0$, then the system (2.13) has a unique equilibrium point. If $r > 0, s > 0$, the equilibrium point O is the center; if $r < 0, s < 0$, it is the saddle. Figure 1 demonstrates the phase portrait in this instance.

(b) When $rs < 0$, the system (2.13) has three equilibrium points. If $r < 0, s > 0$, the equilibrium points O and $Q_{1,2}$ serve as a saddle and centers; if $r > 0, s < 0$, they are a center and saddle. In Figure 2, the relevant phase portrait is displayed.

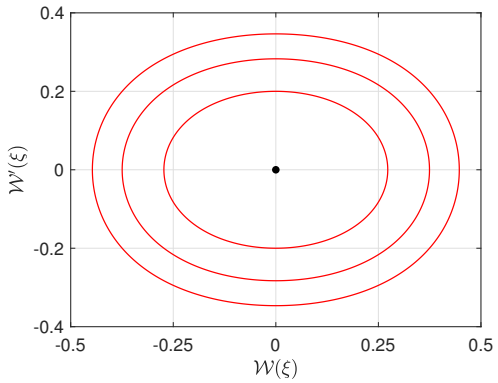

(a) $r > 0, s > 0$

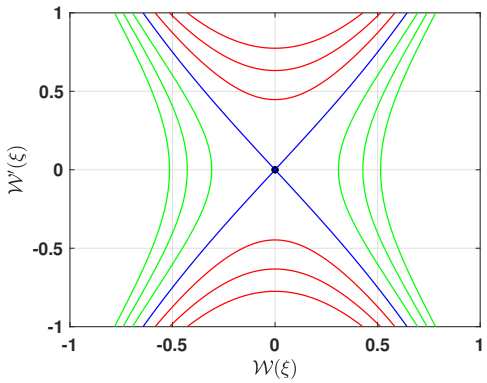

(b) $r < 0, s < 0$

Figure 1. The system (2.13)'s phase portrait for $rs > 0$. The equilibrium point is shown by the black solid point. (a) $r = 1, s = 1$, (b) $r = -1, s = -1$.

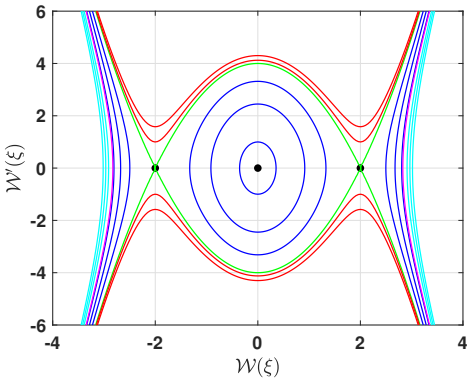

(a) $r > 0, s < 0$

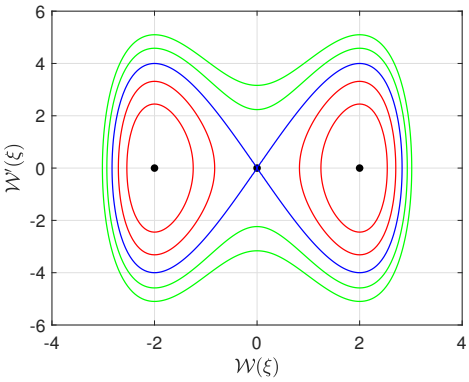

(b) $r < 0, s > 0$

Figure 2. Phase portrait for the system (2.13) for $rs < 0$. The black solid points indicate the equilibrium points. (a) $r = 2, s = -1$, (b) $r = -2, s = 1$.

To give a short description of the phase portrait, we compute the value of the parameter p at the equilibrium points. They are

$$p_0 = \mathcal{H}(O) = 0, \qquad p_1 = \mathcal{H}(Q_{1,2}) = -\frac{r^2}{4s}. \tag{3.3}$$

It is well known that the phase orbits are parametrized by p, i.e.,

$$C_p = \{(\mathcal{W}, \mathcal{W}') \in \mathbb{R}^2 : \mathcal{Y}^2 = 2(p - V(\mathcal{W})\}. \tag{3.4}$$

For fixed values of r and s, the type of solution is determined by the value of p. When $(r, s) \in \mathbb{R}^+ \times \mathrm{R}^+$, all the phase orbits are bounded and periodic for $p > 0$ and they are characterized by $C_{p>0}$. This family of orbits degenerates into the equilibrium point O as p approaches zero; see Figure 1(a). Conversely, if $(r, s) \in \mathbb{R}^- \times \mathrm{R}^-$, all phase orbits are unbounded, as illustrated in Figure 1(b).

Consequently, the corresponding solutions to system (2.13) are also unbounded, making this type of solution physically less significant. When $(r, s) \in \mathbb{R}^+ \times \mathrm{R}^-$, the phase portrait is depicted in Figure 2(a). The type of solution depends on p. There are three families of orbits: the blue family, $C_{0<p<p_1}$, which includes a periodic orbit contained within the heteroclinic orbit in green, $C_{p=p_1}$. For other values of p, the phase orbits are unbounded. Notably, the periodic family in blue degenerates into the equilibrium point O as p approaches zero and into the heteroclinic orbit in green as p approaches p_1. If $(r, s) \in \mathbb{R}^- \times \mathrm{R}^+$, the phase portrait is shown in Figure 2(b). When $p = 0$, a homoclinic orbit appears in blue, $C_{p=0}$, enclosing two periodic families of orbits in red around the two center points $Q_{1,2}$. Additionally, a family of super-periodic orbits emerges in green, $C_{p>0}$. The two periodic orbit families in red degenerate into the equilibrium points $Q_{1,2}$ and into the homoclinic orbit as p approaches p_1 and zero, respectively. On the other hand, the super-periodic family in green degenerates into the blue homoclinic orbit as p approaches zero.

Therefore, the bifurcation parameter p plays a crucial role in determining the solution's behavior.

4. Solutions of SNLKE

The construction of the solution to Eq (1.1), or the determination of $\mathcal{W}(\xi)$, is the main goal of this section. We limit ourselves to forming solutions that correspond to constrained phase orbits in the following. We create the following potential solutions while accounting for the bifurcation conditions on the parameters s, r, and p:

(a) If $r > 0, s > 0, p > 0$, the system has a family of periodic orbits in red as shown in Figure 1(a). Therefore, the polynomial $f(\mathcal{W})$ has two real roots, denoted by $\pm q_1$, and two pure imaginary roots, denoted by $\mathrm{i}q_2$. Hence, $f(\mathcal{W}) = \sqrt{\frac{s}{2}}(q_1^2 - \mathcal{W}^2)(q_2^2 + \mathcal{W}^2)$. Let $\mathcal{W} \in (-q_1, q_1)$ and assume $\mathcal{W}(0) = q_1$. The integration of Eq (2.17) gives

$$\mathcal{W}_1(\xi) = q_1 \mathrm{cn}\Big(\sqrt{\frac{s}{2}(q_1^2 + q_2^2)}\xi, \frac{q_1}{\sqrt{q_1^2 + q_2^2}}\Big), \tag{4.1}$$

where $\mathrm{cn}(u, k)$ is a Jacobi elliptic function [28]. By using Eqs (4.1) and (2.1), Eq (1.1) has a new solution in the form

$$\mathcal{G}_1(x, t) = q_1 \mathrm{cn}\Big(\sqrt{\frac{s}{2}(q_1^2 + q_2^2)}\xi, \frac{q_1}{\sqrt{q_1^2 + q_2^2}}\Big) e^{i\Theta + \sigma\mathcal{B}(t) - \sigma^2 t}. \tag{4.2}$$

Figure 3 provides a graphical representation of solution (4.2) for different values of the noise strength. In Figure 3(a), the solution (4.2) exhibits periodic behavior in the deterministic case. As the noise strength increases, the surface representing the solution becomes rougher, as shown in Figures 3(b)–3(e). Figure 3(f) presents a 2D representation of the solutions, highlighting that an increase in noise strength leads to a decrease in both the amplitude and width of the solution. Moreover, for larger noise values, the solution loses its periodicity.

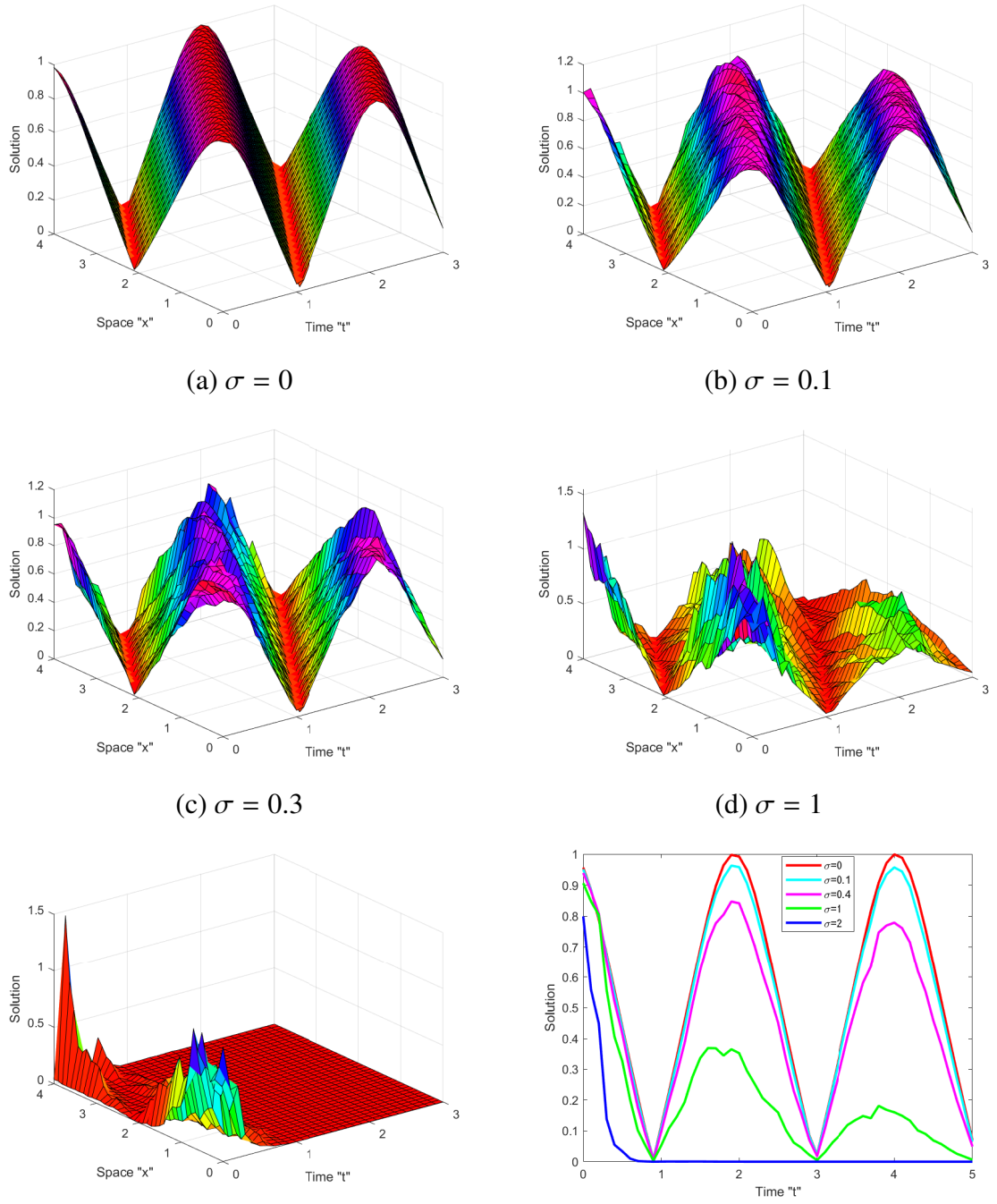

(a) $\sigma = 0$ (b) $\sigma = 0.1$

(c) $\sigma = 0.3$ (d) $\sigma = 1$

(e) $\sigma = 2$ (f) $\sigma = 0,\ 0.1,\ 0.3,\ 1,\ 2$

Figure 3. (a-e) depict 3D-profile of $|\mathcal{G}_1(x,t)|$ presented in Eq (4.2) with $\ell_1 = \theta_1 = -1,\ \ell_2 = \ell_3 = \xi_1 = 1$, and $\xi_2 = -2$ (f) exhibits 2D-profile of Eq (4.2) with various σ.

(b) Figure 2(a) displays the phase picture of the system (2.13) if $r > 0, s < 0$. The phase plane orbits change according to the value of the parameter p, as previously mentioned. As a result, we create potential solutions for $\mathcal{W}(\xi)$ for various p values.

- If $p \in (0, p_1)$, the polynomial $f(\mathcal{W})$ has four real roots, namely, $\pm q_3, \pm q_4$, where $0 < q_3 < q_4$. Hence, it reads as $f(\mathcal{W}) = -\frac{s}{2}(\mathcal{W}^2 - q_3^2)(\mathcal{W}^2 - q_4^2)$. The interval of real solutions for $\mathcal{W}(\xi)$ is $\mathcal{W} \in (-\infty, -q_4) \cup (-q_3, q_3) \cup (q_4, \infty)$. Let us find the solutions along each interval individually.
(i) Presume that $\mathcal{W} \in (-q_3, q_3)$, which represents the blue periodic orbit family. Assuming $\mathcal{W}(0) = q_3$ and integrating both sides of Eq (2.17), we obtain

$$\mathcal{W}_2(\xi) = \pm q_3 \mathrm{cd}\Big(q_4 \sqrt{\frac{-s}{2}}\xi, \frac{q_3}{q_4}\Big). \tag{4.3}$$

The function $\mathrm{cd}(u, k) = \mathrm{cn}(u, k)/\mathrm{dn}(u, k)$ denotes a Jacobi elliptic function [28]. A novel solution to Eq (2.1) can be obtained by substituting the expression (2.12) into (2.1). This solution takes the form

$$\mathcal{G}_2(x, t) = \pm q_3 cd\Big(q_4 \sqrt{\frac{-s}{2}}\xi, \frac{q_3}{q_4}\Big)e^{i\Theta + \sigma\mathcal{B}(t) - \sigma^2 t}. \tag{4.4}$$

(ii) Let $\mathcal{W} \in (q_4, \infty) \cup (-\infty, -q_4)$, which corresponds to the two unbounded orbits in blue. Presuming $\mathcal{W}(0) = q_4$, and both sides of Eq (2.17) are integrated, the result is

$$\mathcal{W}_3(\xi) = \pm q_4 \mathrm{dc}\Big(q_4 \sqrt{\frac{-s}{2}}\xi, \frac{q_3}{q_4}\Big), \tag{4.5}$$

where $\mathrm{dc}(u, k) = \mathrm{dn}(u, k)/\mathrm{cn}(u, k)$ is a Jacobi elliptic function [28]. By substituting the expression (4.5) into Eq (2.1), we obtain a new solution to Eq (1.1) in the form

$$\mathcal{G}_3(x, t) = \pm q_4 \mathrm{dc}\Big(q_4 \sqrt{\frac{-s}{2}}\xi, \frac{q_3}{q_4}\Big)e^{i\Theta + \sigma\mathcal{B}(t) - \sigma^2 t}. \tag{4.6}$$

- On $p = p_1$, the polynomial $f(\mathcal{W})$ has two doubles roots, which are the $\mathcal{W}$-coordinates of the saddle equilibrium points. Hence, it is expressed as $f(\mathcal{W}) = -\frac{s}{2}(\mathcal{W}^2 + \frac{r}{s})^2$. The intervals of real solutions for $\mathcal{W}(\xi)$ are $\mathcal{W} \in (-\infty, -\sqrt{\frac{-r}{s}}) \cup (-\sqrt{\frac{-r}{s}}, \sqrt{\frac{-r}{s}}) \cup (\sqrt{\frac{-r}{s}}, \infty)$. Let us find the solution along each interval individually:
(i) We consider $\mathcal{W} \in \Big(-\sqrt{\frac{-r}{s}}, \sqrt{\frac{-r}{s}}\Big)$, which represents the green heteroclinic orbit connecting the two saddle points $Q_{1,2}$ with themselves. By assuming that $\mathcal{W}(0) = 0$ and both sides of Eq (2.17) are integrated, the result is

$$\mathcal{W}_4(\xi) = \pm \sqrt{\frac{-r}{s}} \tanh\Big(\sqrt{\frac{r}{2}}\xi\Big). \tag{4.7}$$

Inserting the expression (4.7) into Eq (1.1), we obtain a new solution to Eq (1.1) in the form

$$\mathcal{G}_4(x, t) = \pm \sqrt{\frac{-r}{s}} \tanh\Big(\sqrt{\frac{r}{2}}\xi\Big)e^{i\Theta + \sigma\mathcal{B}(t) - \sigma^2 t}. \tag{4.8}$$

Figure 4 provides a graphical representation of the solution (4.8) for various values of the noise strength.
(ii) The two extensions of the hetroclinic orbit are represented by $\mathcal{W} \in (-\infty, -\sqrt{\frac{-r}{s}}) \cup (\sqrt{\frac{-r}{s}}, \infty)$. With the assumption that $\mathcal{W}(0) = \infty$, both sides of Eq (2.17) are integrated; the result is

$$\mathcal{W}_5(\xi) = \mp \sqrt{\frac{r}{s}} \coth\Big(\sqrt{\frac{-r}{2}}\xi\Big). \tag{4.9}$$

We establish a new solution to Eq (1.1) using Eqs (4.9) and (2.1), which takes the form

$$\mathcal{G}_5(x,t) = \mp\sqrt{\frac{r}{s}}\coth\Big(\sqrt{\frac{-r}{2}}\xi\Big)e^{i\Theta+\sigma\mathcal{B}(t)-\sigma^2 t}. \tag{4.10}$$

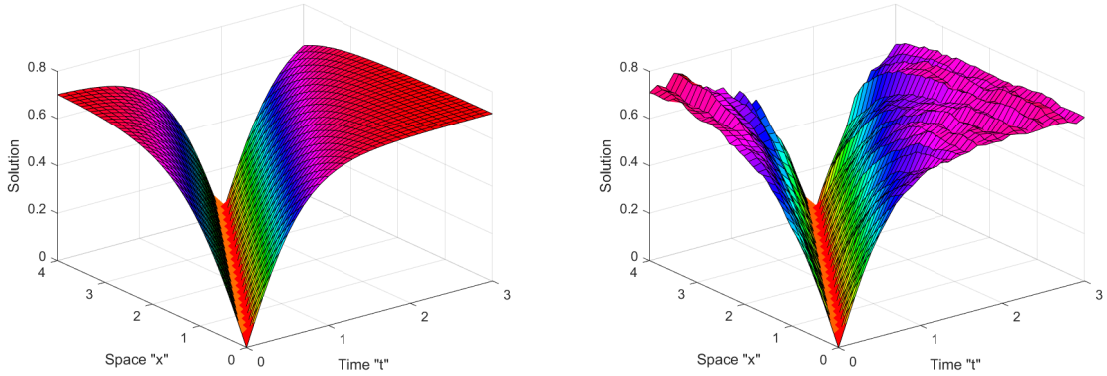

(a) $\sigma = 0$ (b) $\sigma = 0.1$

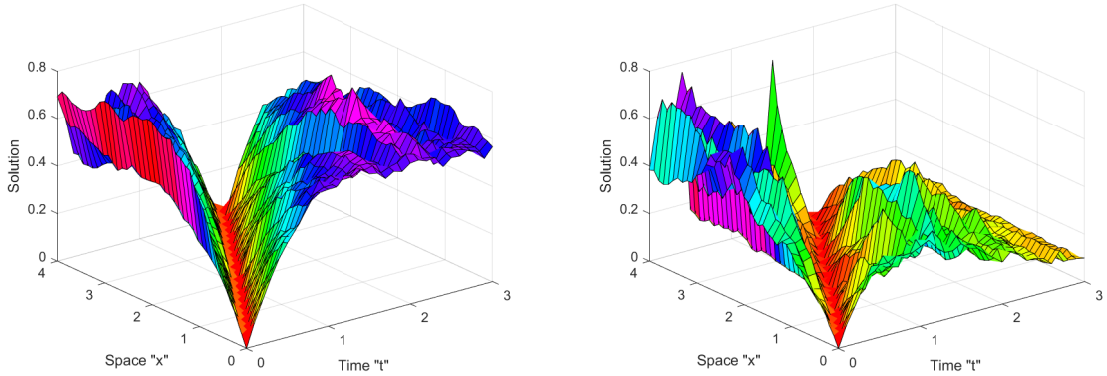

(c) $\sigma = 0.3$ (d) $\sigma = 1$

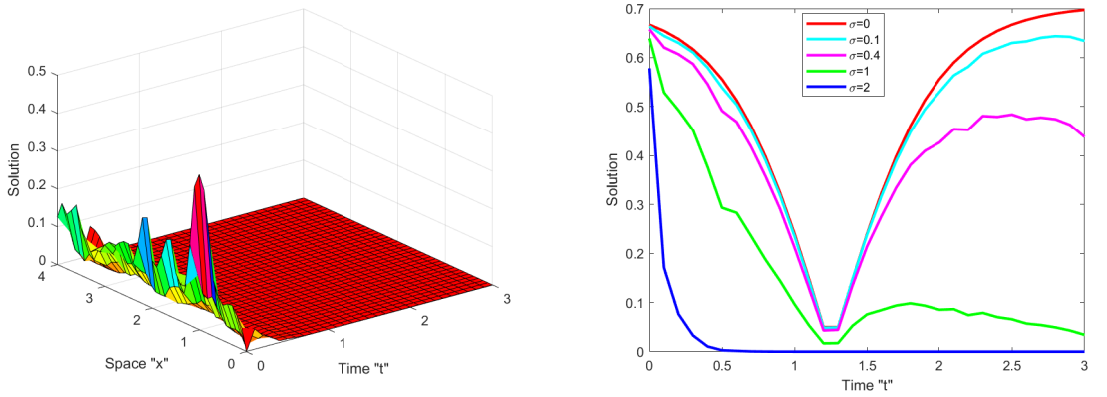

(e) $\sigma = 2$ (f) $\sigma = 0,\ 0.1,\ 0.3,\ 1,\ 2$

Figure 4. (a-e) depict 3D-profile of $|\mathcal{G}_4(x,t)|$ presented in Eq (4.8) with $\ell_1 = \theta_1 = -1,\ \ell_2 = \ell_3 = \xi_1 = 1$, and $\xi_2 = -2$ (f) exhibits 2D-profile of Eq (4.8) with various σ.

- If $p > p_1$, the polynomial $f(\mathcal{W})$ has pure complex conjugate roots denoted by $\pm iq_5$ and $\pm iq_6$, where $0 < q_5 < q_6$. Therefore, we write as $f(\mathcal{W}) = -\frac{s}{2}(\mathcal{W}^2 + q_5^2)(\mathcal{W}^2 + q_6^2)$. The intervals of real solutions for $\mathcal{W}$ are $\mathcal{W} \in (-\infty, \infty)$. Assuming $\mathcal{W}(0) = 0$ and both sides of Eq (2.17) are integrated, the result is

$$\mathcal{W}_6(\xi) = \pm q_5 \mathrm{sc}\Big(q_6 \sqrt{\frac{-s}{2}}\xi, \sqrt{1 - \frac{q_5^2}{q_6^2}}\Big), \tag{4.11}$$

where $\mathrm{sc}(u, k) = \mathrm{sn}(u, k)/\mathrm{cn}(u, k)$ is a Jacobi elliptic function. A newly discovered solution to Eq (1.1) can be obtained by inputting the expression (4.11) into Eq (2.1). This solution takes the form

$$\mathcal{G}_6(x, t) = \pm q_5 \mathrm{sc}\Big(q_6 \sqrt{\frac{-s}{2}}\xi, \sqrt{1 - \frac{q_5^2}{q_6^2}}\Big) e^{i\Theta + \sigma\mathcal{B}(t) - \sigma^2 t}. \tag{4.12}$$

- As shown in Figure 2(a), when $p = 0$, the system (2.13) exhibits a pink unbounded orbit. The polynomial $f(\mathcal{W})$ has two double roots and two simple roots at the origin, $\pm\sqrt{\frac{-r}{2s}}$. The solutions for $\mathcal{W}(\xi)$ are found within the intervals $\mathcal{W} \in (-\infty, -\sqrt{\frac{-r}{2s}}) \cup (\sqrt{\frac{-r}{2s}}, \infty)$. Assuming $\mathcal{W}(0) = 0$ and integrating both sides of Eq (2.1), we derive the following:

$$\mathcal{W}_7(\xi) = \pm\sqrt{\frac{-2r}{s}} \tan(\sqrt{r}\xi). \tag{4.13}$$

We gain a new solution to Eq (1.1) by entering Eq (4.13) into Eq (2.1), which takes the form

$$\mathcal{G}_7(x, t) = \pm\sqrt{\frac{-2r}{s}} \tan(\sqrt{r}\xi) e^{i\Theta + \sigma\mathcal{B}(t) - \sigma^2 t}. \tag{4.14}$$

- When $p < 0$, the polynomial has two real roots, namely $\pm q_7$, and two pure conjugate complex roots, namely $\pm iq_8$. Consequently, $f(\mathcal{W})$ has the structure $f(\mathcal{W}) = -\frac{s}{2}(\mathcal{W}^2 - q_7^2)(\mathcal{W}^2 + q_8^2)$. The real solutions for $\mathcal{W}(\xi)$ exist when $\mathcal{W} \in (q_7, \infty) \cup (-\infty, -q_7)$. Postulating $\mathcal{W}(0) = q_7$ and integrating both sides of Eq (2.1), we obtain

$$\mathcal{W}_8(\xi) = q_7 \mathrm{nc}\Big(\sqrt{\frac{-s}{2}(q_7^2 + q_8^2)}\xi, \frac{q_8}{\sqrt{q_7^2 + q_8^2}}\Big), \tag{4.15}$$

where $\mathrm{nc}(u, k) = 1/\mathrm{cn}(u, k)$ is a Jacobi-elliptic function [28]. By employing the Eqs (4.15) and (2.1), we obtain a novel solution to Eq (1.1) in the form

$$\mathcal{G}_8(x, t) = q_7 \mathrm{nc}\Big(\sqrt{\frac{-s}{2}(q_7^2 + q_8^2)}\xi, \frac{q_8}{\sqrt{q_7^2 + q_8^2}}\Big) e^{i\Theta + \sigma\mathcal{B}(t) - \sigma^2 t}. \tag{4.16}$$

(c) If $r < 0$ and $s > 0$, the phase portrait of system (2.13) is described by Figure 2(b). Let us form the solutions to Eq (1.1) for distinct values of the parameter p, separately.

- A family of super-periodic orbits in green appears in the system when $p > 0$. As a result, the polynomial $f(\mathcal{W})$ has two real roots, $\pm q_9$, and two conjugate pure complex roots, $\pm iq_{10}$. The

formula for $f(\mathcal{W})$ is given by $f(\mathcal{W}) = \frac{s}{2}(q_9^2 - \mathcal{W}^2)(q_{10}^2 + \mathcal{W}^2)$. When $\mathcal{W} \in (-q_9, q_9)$, $\mathcal{W}(\xi)$ has a real solution. Assuming $\mathcal{W}(0) = q_9$ and integrating both sides of Eq (2.1), we obtain

$$\mathcal{W}_9 = q_9 \mathrm{cn}\Big(\sqrt{\frac{s}{2}(q_9^2 + q_{10}^2)}\xi, \frac{q_9}{q_9^2 + q_{10}^2}\Big). \tag{4.17}$$

Using Eqs (4.17) and (2.1), we obtain a new solution to Eq (1.1) in the form

$$\mathcal{G}_9(x,t) = q_9 \mathrm{cn}\Big(\sqrt{\frac{s}{2}(q_9^2 + q_{10}^2)}\xi, \frac{q_9}{q_9^2 + q_{10}^2}\Big)e^{i\Theta + \sigma\mathcal{B}(t) - \sigma^2 t}. \tag{4.18}$$

- When $p \in (p_1, 0)$, the polynomial $f(\mathcal{W})$ has four real roots denoted by $\pm q_{11}$ and $\pm q_{12}$, where $0 < q_{11} < q_{12}$. Hence, it is written as $f(\mathcal{W}) = \frac{s}{2}(q_{11}^2 - \mathcal{W}^2)(\mathcal{W}^2 - q_{12}^2)$. The real solutions for $\mathcal{W}(\xi)$ exist for $\mathcal{W} \in (q_{11}, q_{12}) \cup (-q_{12}, -q_{11})$. Assuming $\mathcal{W}(0) = q_{12}$ and integrating both sides of Eq (2.1), we obtain

$$\mathcal{W}_{10}(\xi) = \pm q_{12} \mathrm{dn}(q_{12}\sqrt{\frac{s}{2}}\xi, \sqrt{1 - \frac{q_{11}^2}{q_{12}^2}}). \tag{4.19}$$

Inserting the expression (4.19) into Eq (2.1), we obtain a novel solution to Eq (1.1) in the form

$$\mathcal{G}_{10}(x,t) = \pm q_{12} \mathrm{dn}\Big(q_{12}\sqrt{\frac{s}{2}}\xi, \sqrt{1 - \frac{q_{11}^2}{q_{12}^2}}\Big)e^{i\Theta + \sigma\mathcal{B}(t) - \sigma^2 t}. \tag{4.20}$$

- When $p = 0$, the system (2.13) has two homoclinic orbits in blue connected to the saddle point O with itself. The polynomial $f(\mathcal{W})$ has two simple roots, $\pm\sqrt{\frac{-2r}{s}}$, and one double root at the origin. Therefore, it is written as $f(\mathcal{W}) = \frac{s}{2}\mathcal{W}^2(\frac{-2r}{s} - \mathcal{W}^2)$. The real solution for $\mathcal{W}$ exists if $\mathcal{W} \in (0, \sqrt{\frac{-2r}{s}}) \cup (-\sqrt{\frac{-2r}{s}}, 0)$. Let $\mathcal{W} \in (0, \sqrt{\frac{-2r}{s}})$, which corresponds to the right homoclinic orbit, and assume $\mathcal{W}(0) = \sqrt{\frac{-2r}{s}}$. Hence, the integration of both sides of Eq (2.1) gives

$$\mathcal{W}_{11}(\xi) = \sqrt{\frac{2r}{-s}}\mathrm{sech}(\sqrt{-r}\xi). \tag{4.21}$$

By utilizing the Eqs (4.21) and (2.1), we obtain a new solution to Eq (1.1) in the form

$$\mathcal{G}_{11}(x,t) = \sqrt{\frac{2r}{-s}}\mathrm{sech}(\sqrt{-r}\xi)e^{i\Theta + \sigma\mathcal{B}(t) - \sigma^2 t}. \tag{4.22}$$

Figure 5 provides a graphical representation of the solution (4.22) for different values of noise strength. Figure 5(a) illustrates that the surface representing the solution (4.22) is solitary and smooth. As the noise strength σ increases, the surface characterizing the solution (4.22) becomes rough, as shown in Figures 5(b) and 5(c). Furthermore, for larger noise values, the solution (4.22) flattens, as depicted in Figure 5(d). The 2D representation of the solution (4.22) shows that while the amplitude decreases, the width remains approximately unchanged. However, for larger noise values, the solution (4.22) becomes completely flat, as illustrated in Figure 5(f).

Remark 4.1. *We observe that the solutions of the SNLKE (1.1) fluctuate and have a distinct pattern when the noise strength $\sigma = 0$. However, as the noise strength σ increases, the pattern begins to break down, as shown in Figures 3–5. This indicates that the multiplicative noise in the Itô sense affects the solutions of the SNLKE (1.1) and stabilizes them around zero.*

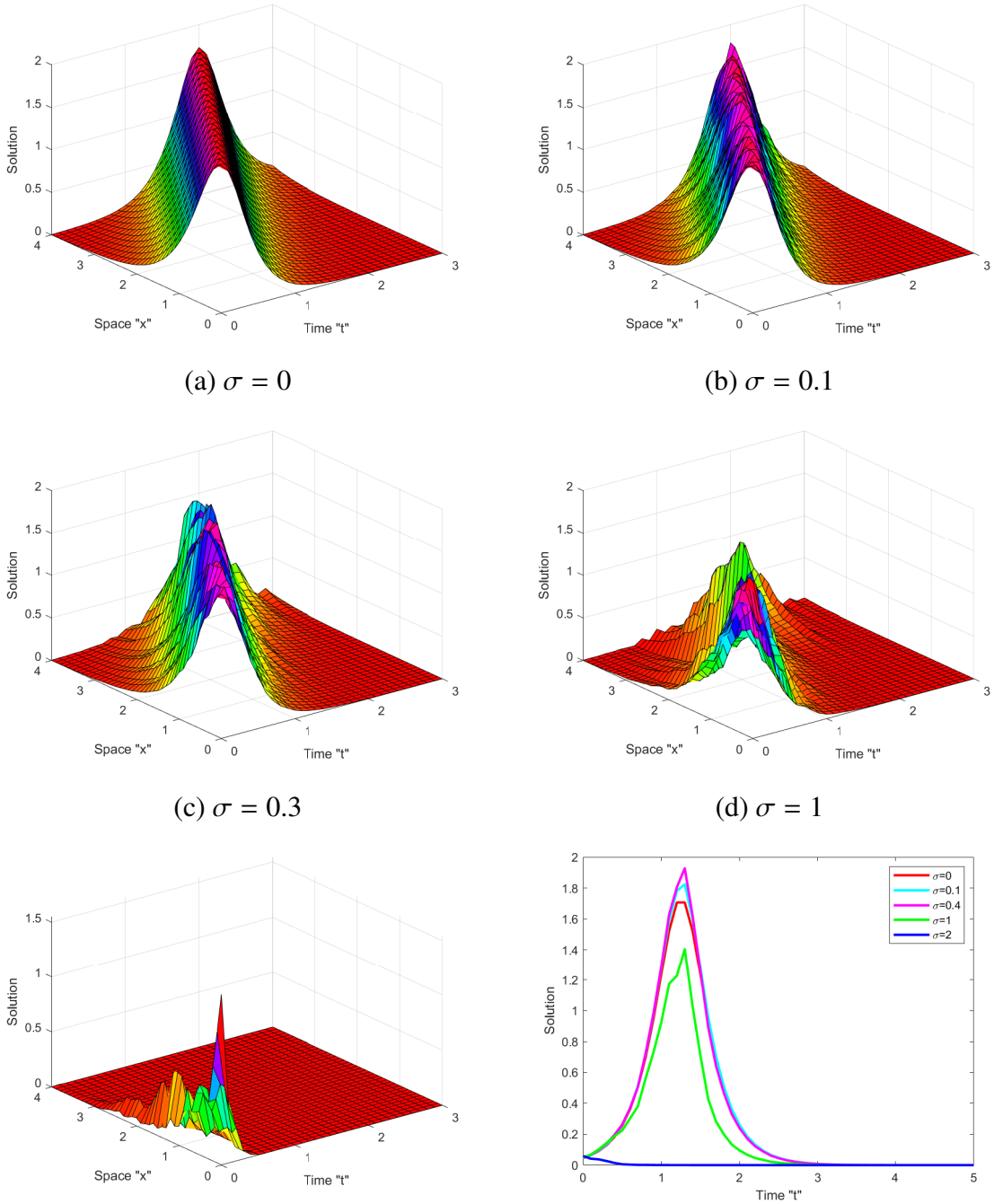

(a) $\sigma = 0$ (b) $\sigma = 0.1$

(c) $\sigma = 0.3$ (d) $\sigma = 1$

(e) $\sigma = 2$ (f) $\sigma = 0,\ 0.1,\ 0.3,\ 1,\ 2$

Figure 5. (a-e) depict 3D-profile of $|\mathcal{G}_{11}(x,t)|$ presented in Eq (4.22) with $\theta_1 = \ell_1 = \ell_2 = \ell_3 = \xi_1 = 1$, and $\xi_2 = -2$ (f) exhibits 2D-profile of Eq (4.22) with various σ.

5. Quasi-periodic behaviour

This section looks at the non-autonomous system's autoresonance behaviour, or how the oscillator self-regulates when it is exposed to a fluctuating periodic force. Thus, we consider the perturbed system

$$\begin{aligned} \mathcal{W}' &= \mathcal{Y}, \\ \mathcal{Y}' &= -\mathcal{W}(r + s\mathcal{W}^2) + \nu_1 \mathrm{cn}(\nu_2 \xi, \kappa). \end{aligned} \tag{5.1}$$

The external effects denoted by $F = \nu_1 \mathrm{cn}(\nu_2 \xi, \kappa)$ are defined by the two parameters ν_i, $i = 1, 2$. Strength and frequency of external periodic effects F are indicated by the parameters ν_1 and ν_2. The period of the external effect is $4K(\kappa)/\nu_2$, where $K(\kappa)$ is a complete elliptic integral of the first kind and given by [28]

$$K(\kappa) = \int_0^{\pi/2} \frac{\mathrm{d}\psi}{\sqrt{1 - \kappa^2 \sin^2 \psi}}.$$

The perturbed system can be viewed as a generalization of the undamped Duffing system [29], to which it reduces when $\kappa = 0$. The presence of the arbitrary constants r and s, along with the two constants ν_1, ν_2, and κ that define the perturbed term, complicates the analysis of the periodic and chaotic dynamical features of the system (5.1). This analysis includes varying the frequency and strength while keeping the other parameters constant.

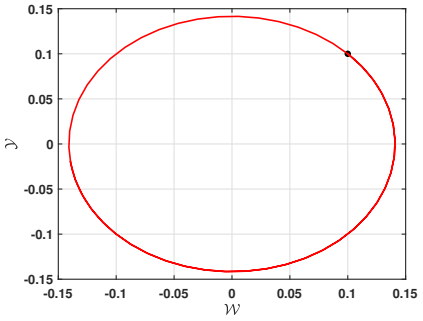

(a) $2D-$ phase portrait

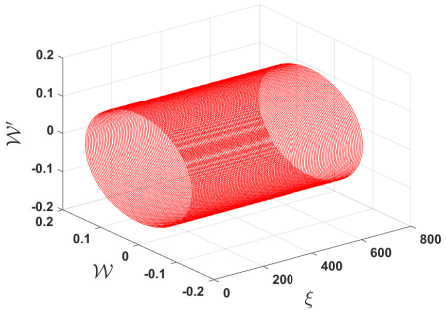

(b) $3D-$ phase portrait

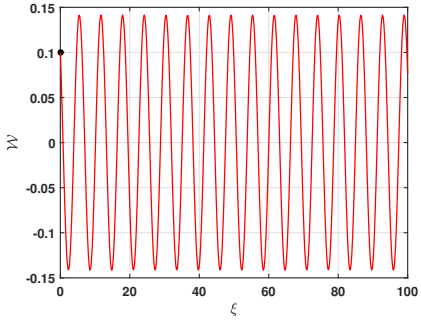

(c) Time analysis $\mathcal{W}(\xi)$ verse ξ

Figure 6. The 2D, 3D, and time series for the unperturbed system (2.13) with initial condition $\mathcal{W}(0) = 0.1$ and $\mathcal{W}'(0) = 0.1$ while $r = 1$, $s = 1$, and $\kappa = 0.02$.

First, we analyze the perturbed system (5.1) with $\nu_1 = 0$, which is equivalent to considering the unperturbed system (2.13). Based on the bifurcation analysis, the unperturbed system (2.13) exhibits periodic behavior when $(r, s, p) \in (\mathbb{R}^+ \times \mathbb{R}^+ \times \mathbb{R}^+) \cup (\mathbb{R}^+ \times \mathbb{R}^- \times (0, -\frac{r^2}{4s})) \cup (\mathbb{R}^- \times \mathbb{R}^+ \times (-\frac{r^2}{4s}, 0))$. In this study, we focus on the case $(r, s, p) \in (\mathbb{R}^+ \times \mathbb{R}^+ \times \mathbb{R}^+)$, as the similarity in the analysis for the other possible ranges of r, s, and p. Accordingly, we set $r = 1$ and $s = 1$. Choosing initial conditions $\mathcal{W}(0) = 0.1$ and $\mathcal{W}'(0) = 0.1$ and applying Eq (2.16), we obtain $p = 0.100025 > 0$. Thus, for these parameter values and initial conditions, the unperturbed system (2.13) exhibits periodic behavior, as illustrated in Figure 6, in agreement with the bifurcation theory. The system exhibits a periodic phase orbit as shown in Figures 6(a) and 6(b). Additionally, Figure 6(c) illustrates the periodicity of $\mathcal{W}(\zeta)$ versus ζ.

Second, we analyze the perturbed system (5.1) using the same values for r, s, κ, and the initial conditions, in order to investigate the influence of periodic external effects on the dynamical behavior of system (2.13).

By choosing $\nu_1 = 0.2$, $\nu_2 = \sqrt{3}$, $\kappa = 0.02$, the 2D and 3D phase portraits shown in Figures 7(a) and 7(b) exhibit a regular structure (e.g., invariant tori), indicating the presence of quasi-periodicity. This behavior is further confirmed by the time series displayed in Figure 7(c).

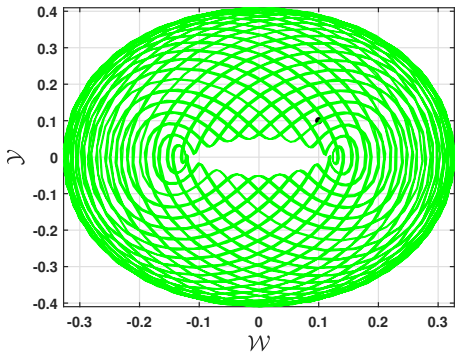

(a) $2D-$ phase portrait

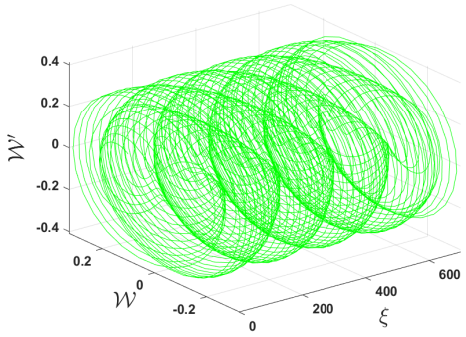

(b) $3D-$ phase portrait

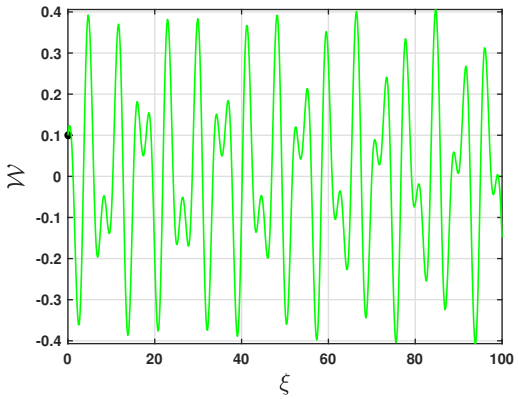

(c) Time analysis $\mathcal{W}(\xi)$ verse ξ

Figure 7. The 2D, 3D, and time series for the unperturbed system (5.1) with initial condition $\mathcal{W}(0) = 0.1$ and $\mathcal{W}'(0) = 0.1$ while $r = 1$, $s = 1$, $\nu_1 = 0.2$, $\nu_2 = \sqrt{3}$, and $\kappa = 0.02$.

In a contrast, When $\nu_1 = 20, \nu_2 = 1, \kappa = 0.02$, the 2D and 3D phase portraits shown in Figures 8(a) and 8(b) display irregular dynamics, indicating the presence of chaotic behavior. This is further illustrated by the time series presented in Figure 8(c).

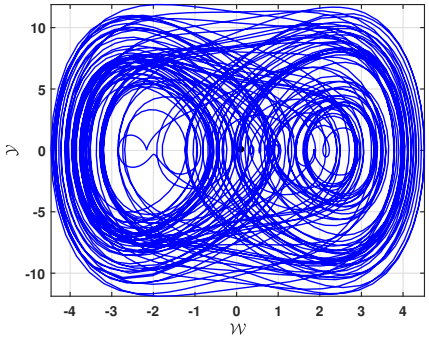

(a) $2D-$ phase portrait

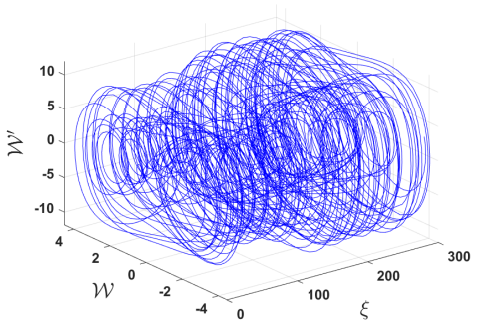

(b) $3D-$ phase portrait

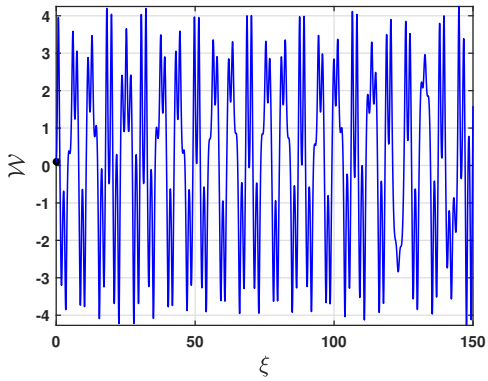

(c) Time analysis $\mathcal{W}(\xi)$ verse ξ

Figure 8. The 2D, 3D, and time series for the unperturbed system (5.1) with initial condition $\mathcal{W}(0) = 0.1$ and $\mathcal{W}'(0) = 0.1$ while $r = 1, s = 1, \nu_1 = 20, \nu_2 = 1$, and $\kappa = 0.02$.

On another hand, the Poincaré surface of section is a powerful tool for the qualitative analysis of dynamical systems, particularly in studying nonlinear and Hamiltonian systems. This method records the intersections of a trajectory with a lower-dimensional subspace (the "section") at discrete time intervals, effectively reducing the system's dimensionality. By doing so, it enables clearer visualization of long-term behavior. Distinct patterns on the section, such as regular, quasi-periodic, or chaotic dynamics, can be readily identified and analyzed [30, 31].

The Poincaré surface of section is generated for the perturbed system using MATLAB, considering different values of the parameters ν_1 and ν_2 using Matlab software. Figure 9 displays the Poincaré surface of section for system (5.1) across varying parameters ν_1, and ν_2. Figure 9(a) ($\nu_1 = 0$) reveals a single line on the section, confirming strictly periodic motion. Figure 9(b), for $\nu_1 = 0.2$, $\nu_2 = \sqrt{3}$, and $\kappa = 0.02$, exhibits points distributed along nested closed curves (invariant tori), indicative of quasi-periodic dynamics. In contrast, Figure 9(c) ($\nu_1 = 20$, $\nu_2 = 1$ and $\kappa = 0.02$) demonstrates a scattered point distribution, a hallmark of chaos. Together, these results illustrate the system's progression from periodic to quasi-periodic and finally to chaotic behavior as parameters are adjusted.

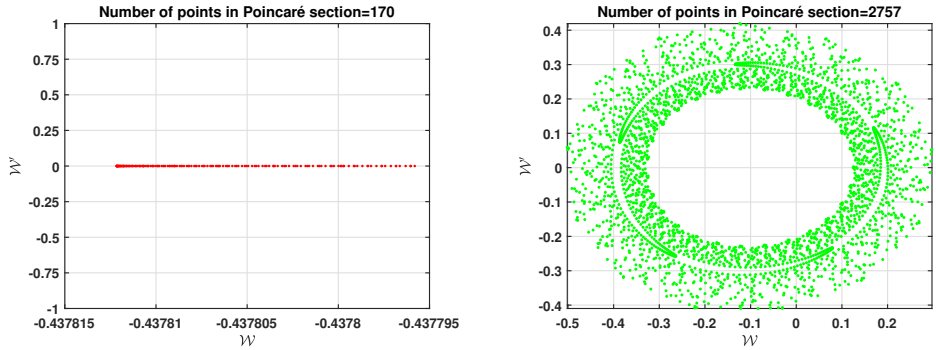

(a) $\nu_1 = 0$ (b) $\nu_1 = 0.2, \nu_2 = \sqrt{3}$

(c) $\nu_1 = 20, \nu_2 = 1$

Figure 9. Poincaré surface of section for the system (5.1) for different values of ν_1 and ν_2.

6. Conclusions

This paper is interested in constructing traveling wave solutions for the stochastic nonlinear Kodama equation (SNLKE) forced by multiplicative white noise. A wave transformation has been applied to transform the SNLKE into a two-dimensional dynamical system. Based on the qualitative theory of the dynamical system, the bifurcation and phase portrait have been investigated and clarified graphically in the phase plane for different values of the parameters. Taking into account the conserved quantity and bifurcation constraints on the parameters, some new traveling wave solutions have been introduced. Furthermore, we have explained the influence of multiplicative noise on the exact solution of the SNLKE graphically. Furthermore, we have explored the quasi-periodic and chaotic patterns exhibited by the perturbed system by introducing periodic external effects into the current phenomenon, thereby illustrating the system's chaotic behavior. Quasi-periodic patterns play a crucial role in designing and optimizing optical systems, influencing key features such as resonance modes, light propagation, and filtering properties. They are particularly important in photonic crystals and integrated optical devices, where precise periodicity control enhances performance and enables new functionalities. Understanding these phenomena can improve the efficiency of optical sensors, modulators, and lasers, as well as optimize light trapping in solar cells and resonance tuning in optical cavities. For further details, see, for example, [32]. In future work, we can consider the stochastic nonlinear Kodama equation with additive noise.

Author contributions

S. T. Obeidat: Methodology, Validation, Formal analysis, Writing original draft preparation, Writing–review and editing; D. Rizk: Methodology, Software, Validation, Formal analysis, Funding acquisition, Writing original draft preparation, Writing–review and editing; W. W. Mohammed: Methodology, Software, Validation, Formal analysis, Writing original draft preparation, Writing–review and editing; A. Elmandouh: Methodology, Software, Validation, Formal analysis, Writing original draft preparation, Writing–review and editing. All authors have read and agreed to the published version of the manuscript.

Use of Generative-AI tools declaration

The authors declare they have not used Artificial Intelligence (AI) tools in the creation of this article.

Acknowledgments

The researchers would like to thank the Deanship of Graduate Studies and Scientific Research at Qassim University for financial support (QU-APC-2025).

Conflict of interest

The authors declare that they have no conflicts of interest.

References

1. L. Arnold, *Random dynamical systems*, Berlin, Heidelberg: Springer, 1998. https://doi.org/10.1007/978-3-662-12878-7
2. W. W. Mohammed, N. Iqbal, T. Botmart, Additive noise effects on the stabilization of fractional-space diffusion equation solutions, *Mathematics*, **10** (2022), 1–14. https://doi.org/10.3390/math10010130
3. K. Khan, M. A. Akbar, The $exp(-\phi(\varsigma))$-expansion method for finding travelling wave solutions of Vakhnenko-Parkes equation, *Int. J. Dyn. Syst. Differ. Equ.*, **5** (2014), 72–83. https://doi.org/10.1504/IJDSDE.2014.067119
4. F. M. Al-Askar, W. W. Mohammed, M. Alshammari, Impact of Brownian motion on the analytical solutions of the space-fractional stochastic approximate long water wave equation, *Symmetry*, **14** (2022), 1–10. https://doi.org/10.3390/sym14040740
5. A. A. Elmandouh, M. E. Elbrolosy, Integrability, variational principle, bifurcation, and new wave solutions for the Ivancevic option pricing model, *J. Math.*, **2022** (2022), 9354856. https://doi.org/10.1155/2022/9354856
6. M. M. El-Dessoky, A. Elmandouh, Qualitative analysis and wave propagation for Konopelchenko-Dubrovsky equation, *Alex. Eng. J.*, **67** (2023), 525–535. https://doi.org/10.1016/j.aej.2022.12.066

7. I. Siddique, K. B. Mehdi, F. Jarad, M. E. Elbrolosy, A. A. Elmandouh, Novel precise solutions and bifurcation of traveling wave solutions for the nonlinear fractional (3+1)-dimensional WBBM equation, *Int. J. Mod. Phys. B*, **37** (2023), 2350011. https://doi.org/10.1142/S021797922350011X
8. A. M. Wazwaz, The sine-cosine method for obtaining solutions with compact and noncompact structures, *Appl. Math. Comput.*, **159** (2004), 559–576. https://doi.org/10.1016/j.amc.2003.08.136
9. M. L. Wang, X. Z. Li, J. L. Zhang, The (G'/G)-expansion method and travelling wave solutions of nonlinear evolution equations in mathematical physics, *Phys. Lett. A*, **372** (2008), 417–423. https://doi.org/10.1016/j.physleta.2007.07.051
10. W. W. Mohammed, H. Ahmad, A. E. Hamza, E. S. Aly, M. El-Morshedy, E. M. Elabbasy, The exact solutions of the stochastic Ginzburg-Landau equation, *Results Phys.*, **23** (2021), 103988. https://doi.org/10.1016/j.rinp.2021.103988
11. H. M. Baskonus, H. Bulut, T. A. Sulaiman, New complex hyperbolic structures to the Lonngren-wave equation by using sine-gordon expansion method, *Appl. Math. Nonlinear Sci.*, **4** (2019), 129–138. https://doi.org/10.2478/AMNS.2019.1.00013
12. Z. Yan, Abundant families of Jacobi elliptic function solutions of the (2+1)-dimensional integrable Davey-Stewartson-type equation via a new method, *Chaos Solitons Fract.*, **18** (2003), 299–309. https://doi.org/10.1016/S0960-0779(02)00653-7
13. B. Lu, The first integral method for some time fractional differential equations, *J. Math. Anal. Appl.*, **395** (2012), 684–693. https://doi.org/10.1016/j.jmaa.2012.05.066
14. S. Malik, M. S. Hashemi, S. Kumar, H. Rezazadeh, W. Mahmoud, M. S. Osman, Application of new Kudryashov method to various nonlinear partial differential equations, *Opt. Quantum Electron.*, **55** (2023), 8. https://doi.org/10.1007/s11082-022-04261-y
15. S. F. Wang, Novel soliton solutions of CNLSEs with Hirota bilinear method, *J. Opt.*, **52** (2023), 1602–1607. https://doi.org/10.1007/s12596-022-01065-x
16. S. M. Mirhosseini-Alizamini, H. Rezazadeh, M. Eslami, M. Mirzazadeh, A. Korkmaz, New extended direct algebraic method for the Tzitzica type evolution equations arising in nonlinear optics, *Comput. Methods Differ. Equ.*, **8** (2020), 28–53. https://doi.org/10.22034/cmde.2019.9472
17. M. Shakeel, Attaullah, N. A. Shah, J. D. Chung, Application of modified exp-function method for strain wave equation for finding analytical solutions, *Ain Shams Eng. J.*, **14** (2023), 101883. https://doi.org/10.1016/j.asej.2022.101883
18. N. A. Shah, E. R. El-Zahar, A. Akgül, A. Khan, J. Kafle, Analysis of fractional-order regularized long-wave models via a novel transform, *J. Funct. Spaces*, **2022** (2022), 2754507. https://doi.org/10.1155/2022/2754507
19. Y. Kodama, Optical solitons in a monomode fiber, *J. Stat. Phys.*, **39** (1985), 597–614. https://doi.org/10.1007/BF01008354
20. P. Kumari, R. K. Gupt, S. Kumar, K. S. Nisar, Doubly periodic wave structure of the modified Schrödinger equation with fractional temporal evolution, *Results Phys.*, **33** (2022), 105128. https://doi.org/10.1016/j.rinp.2021.105128
21. M. J. Potasek, M. Tabor, Exact solutions for an extended nonlinear Schrödinger equation, *Phys. Lett. A*, **154** (1991), 449–452. https://doi.org/10.1016/0375-9601(91)90971-a

22. K. Hosseini, E. Hincal, S. Salahshour, M. Mirzazadeh, K. Dehingia, B. J. Nath, On the dynamics of soliton waves in a generalized nonlinear Schrödinger equation, *Optik*, **272** (2023), 170215. https://doi.org/10.1016/j.ijleo.2022.170215

23. K. Hosseini, F. Alizadeh, E. Hinçal, D. Baleanu, A. Akgül, A. M. Hassan, Lie symmetries, bifurcation analysis, and Jacobi elliptic function solutions to the nonlinear Kodama equation, *Results Phys.*, **54** (2023), 107129. https://doi.org/10.1016/j.rinp.2023.107129

24. W. W. Mohammed, N. Iqbal, R. Sidaoui, E. E. Ali, Dynamical behavior of the fractional nonlinear Kadoma equation in plasma physics and optics, *Mod. Phys. Lett. B*, **39** (2024), 2450434. https://doi.org/10.1142/S0217984924504347

25. M. S. Algolam, A. I Ahmed, H. M. Alshammary, F. E Mansour, W. W Mohammed, The impact of standard Wiener process on the optical solutions of the stochastic nonlinear Kodama equation using two different methods, *J. Low Freq. Noise Vib. Active Control*, **43** (2024), 1939–1952. https://doi.org/10.1177/14613484241275313

26. O. Calin, *An informal introduction to stochastic calculus with applications*, World Scientific, 2015. https://doi.org/10.1142/9620

27. H. Goldstein, *Classical mechanics*, 3 Eds., Addison-Wesley, 2001.

28. P. F. Byrd, M. D. Friedman, *Handbook of elliptic integrals for engineers and scientists*, Berlin, Heidelberg: Springer, 1971. https://doi.org/10.1007/978-3-642-65138-0

29. M. Lakshmanan, S. Rajaseekar, *Nonlinear dynamics: integrability, chaos and patterns*, Berlin, Heidelberg: Springer, 2012.

30. E. Ott, *Chaos in dynamical systems*, Cambridge University Press, 2002. https://doi.org/10.1017/CBO9780511803260

31. S. Wiggins, *Introduction to applied nonlinear dynamical systems and chaos*, New York: Springer, 2003. https://doi.org/10.1007/b97481

32. M. Debnath, A. R. Chowdhury, Period doubling and hysteresis in a periodically forced, damped anharmonic oscillator, *Phys. Rev. A*, **44** (1991), 1049. https://doi.org/10.1103/PhysRevA.44.1049

AIMS Press